Catalysis Today 175 (2011) 48–54

Contents lists available at ScienceDirect

Catalysis Today

journal homepage: www.elsevier.com/locate/cattod

Morphology and nanosize effects of ceria from different precursors on the activity for NO reduction

Lianjun Liu[a], Yuan Cao[a], Wenjing Sun[a], Zhijian Yao[a], Bin Liu[a], Fei Gao[b], Lin Dong[a,b,*]

[a] Key Laboratory of Mesoscopic Chemistry of MOE, School of Chemistry and Chemical Engineering, Nanjing University, Nanjing, 210093, PR China
[b] Modern Analysis Center, Nanjing University, Nanjing, 210093, PR China

ARTICLE INFO

Article history:
Received 15 October 2010
Received in revised form 15 February 2011
Accepted 6 April 2011
Available online 23 May 2011

Keywords:
Morphology
CeO_2
Nanosize
Precursor
NO reduction

ABSTRACT

The present work comparatively explored the morphology and size-dependent reduction and activity of CeO_2 nanostructures for NO reduction. CeO_2 nanorods were prepared by $Ce(NO_3)_3$, while spherical-like nanoparticles with an average size of 4–6 nm were obtained from $(NH_4)_2Ce(NO_3)_6$ and $Ce(SO_4)_2$. As compared with CeO_2 nanorods, these nanoparticles (4–6 nm) showed the larger lattice strain and higher activity for NO reduction, which was due to the nanosize effect that significantly improved the intrinsic reducibility of surface oxygen and facilitated the formation of oxygen vacancies. In addition, the adsorption type and configuration of NO was similar over these different shaped ceria. However, CeO_2 nanoparticles from tetravalent cerium showed the greater capacity to activate the adsorbed NO species than nanorods from the tervalent nitrates.

1. Introduction

CeO_2, as a functional material, possesses many attractive properties which make it highly promising for a wide range of applications such as automotive three-way catalysts, solid electrolytes in solid oxide fuel cell, oxygen sensors, irradiation protector, UV block and low temperature Water–gas shift reaction [1]. The importance of ceria for catalytic removal of NO_x, CO and C_xH_y originates from its oxygen storage capability (OSC) and remarkable Ce^{4+}/Ce^{3+} redox in automobile exhaust converters. In addition to the particle size, the morphology also largely influences the repeatable Ce^{4+}/Ce^{3+} redox property and OSC. In this situation, one-dimensional ceria nanostructures had successfully been synthesized and examined in catalytic CO oxidation reaction, such as nanorods [2,3], nanowires [4], nanotubes [5,6] and spheres [7,8]. For example, CeO_2 nanorods, which predominantly exposed the more reactive (1 1 0) and (1 0 0) planes, showed the higher activity for CO oxidation than nanoparticles with the less reactive (1 1 1) planes [1a]. It is generally accepted that the oxidation of CO on ceria involves the participation of lattice oxygen species [4]. In fact, the oxygen species both on the surface and in the bulk could participate in the redox cycle in nanorods, thus giving a much higher OSC and activity. The OSC (in terms of exposed crystal planes) of ceria followed the order of nanocubes > nanorods ≫ nanopolyhedra [3]. Particularly, the quality and types of oxygen species in ceria were determined by its different size [8a]. Thus, the well-defined active sites for catalytic reactions could be achieved by controlling the morphology and size of ceria nanostructures.

Ceria also acted as an important component in NO_x reduction reaction, probably due to the creation of oxygen vacancy for NO adsorption and dissociation [9]. Theoretical calculation showed that the (1 1 0) surface had the lower vacancy formation energy than (1 0 0) and (1 1 1) surfaces [10], indicating its potentially higher ability for NO dissociation. As reported elsewhere [11], the reduction of cerium ions by the introduction of an oxygen vacancy changed the geometry and energy of the system, and the reduced surface of ceria was energetically more favorable than the unreduced surface for oxygen reduction. Analysis of the electronic structure and spin density distributions demonstrated that one Ce^{3+} ion had been reoxidized to Ce^{4+} by NO_2, with the formation of adsorbed NO_2^- [12]. Along this line, the above discussion indicated any processing condition, which favored the formation of more desired oxygen vacancy in ceria, would result in the enhanced reducibility and NO reduction activity. As a result, ceria nanorods prepared from $CeCl_3$ possessed a higher concentration of larger size oxygen vacancy clusters than that from $Ce(NO_3)_3$, which showed the promoting reducibility and activity for CO oxidation [1b]. Furthermore, the rate of NO reduction reaction increased with the increase in oxide ion vacancies by substituting La or Y in CeO_2 with Pt [13]. Another strategy to facilitate the formation of oxygen vacancy is to control the size of ceria within the nanoscale.

* Corresponding author at: Hankou Road 22#, Nanjing, Jiangsu Province, 210093, PR China. Tel.: +86 25 83592290; fax: +86 25 83317761.
E-mail address: donglin@nju.edu.cn (L. Dong).

0920-5861/$ – see front matter.
doi:10.1016/j.cattod.2011.04.018

However, one question that should be addressed is how the cerium precursor influences the shape and size of CeO_2. Importantly, little attention is paid on the investigation of nanoceria with respect to morphology and size effects on NO reduction and adsorption. Therefore, fundamental understanding of this issue is helpful to gain further insight into the intrinsic property of CeO_2 and its application in NO elimination.

In this work, we prepared nanoscale ceria from different cerium precursors, and comparatively studied the shape and size-dependent reduction feature, NO adsorption and activity of ceria nanostructures by XRD, Raman, UV–vis, TEM (HRTEM), H_2-TPR, in situ FTIR and NO + CO model reaction.

2. Experimental

2.1. Catalyst preparation

Nanocrystal CeO_2 with different morphology was prepared by the hydrothermal method. A requisite amount of $Ce(NO_3)_3{\cdot}6H_2O$ (2.0 g) was dissolved into 10 ml distilled water, and then 90 ml NaOH (5 M) was quickly added and kept stirring for 1 h in the Teflon bottle. Subsequently, the bottle was held in a stainless steel vessel autoclave, and the autoclave was sealed tightly. Finally, the autoclave was subjected to hydrothermal treatment at 130 °C for 24 h in a temperature-controlled electric oven. After the hydrothermal treatment, fresh precipitates were separated by centrifugation, washed with deionized water and ethanol until pH 7, and dried at 60 °C in air overnight. The products were calcined at 400 °C (1 °C/min) in the flowing air for 3 h. The same procedure was performed on other cerium precursors (with the same molar amount) like $(NH_4)_2Ce(NO_3)_6$, $Ce(SO_4)_2$ and CeO_2 (obtained by the decomposition of $Ce(NO_3)_3$ at 450 °C in air for 5 h). For simplify, these corresponding CeO_2 powders were denoted as $Ce^{3+}N$, $Ce^{4+}N$, $Ce^{4+}S$ and CeO, respectively.

2.2. Catalyst characterization

XRD patterns were recorded on a Philips X'pert Pro diffractometer using Ni-filtered Cu Kα radiation (λ = 0.15418 nm). The X-ray tube was operated at 40 kV and 40 mA. The mean grain sizes (D_β) from the (1 1 1) plane and strain (ε) of these samples were calculated by the Scherrer equation ($D_\beta = K\lambda/\beta\cos\theta$) and $\varepsilon = \beta/4tg\theta$, respectively.

Raman spectra were collected on a Jobin–Yvon (France–Japan) T64000 type Laser Raman spectroscopy using Ar^+ laser beam, operating with an excitation wavelength of 516 nm and the laser power of 300 mW.

HR-TEM images of these samples were obtained by a JEM-2100CX system. The three samples were dispersed in ethanol and kept in an ultrasonic bath for 15 min, then deposited on a carbon-covered copper grid for measurement.

UV–vis DRS spectra were recorded in the range of 200–900 nm by a UV–vis–NIR 5000 spectrophotometer. $BaSO_4$ was used as the reference for baseline emendation.

H_2-TPR was carried out in a quartz U-tube reactor connected to a thermal conductivity detector with H_2–Ar mixture (7.0% H_2 by volume) as reductant. Before being switched to H_2–Ar stream, 50 mg sample was pretreated in N_2 stream at 400 °C for 1 h. After then, TPR started from room temperature to 900 °C at a rate of 10 °C min^{-1}.

In situ FT-IR spectra were collected from 400 to 4000 cm^{-1} at a resolution 4 cm^{-1} (number of scans, ~32) on a Nicolet 5700FT-IR spectrometer. The catalysts (about 25 mg) were mounted in an IR cell, and pretreated for 1 h at 100 °C in the flowing N_2 atmosphere. After cooled to room temperature, the self-supporting wafer was exposed to a controlled stream of CO–Ar (10% CO) and NO–Ar (5% NO) at a rate of 5.0 ml min^{-1} for 30 min. In situ FT-IR spectra (temperature programmed reaction) were recorded at various target temperatures by subtraction of the background reference (collected from the gas data at each temperature without the samples).

2.3. Catalytic activity tests

The activities of the catalysts were determined under light-off procedure, involving a feed steam with a fixed composition, 5% NO, 10% CO and 85% He by volume as diluents. The catalysts (50 mg) were pretreated in N_2 stream at 100 °C for 1 h, and then the mixed gases were switched on. The reactions were carried out at different temperatures (from 200 to 400 °C) with GHSV = 12,000 h^{-1}. Two gas chromatographs (GC) equipped with thermal conductivity detector were used for analyzing the production, column A with Paropak Q for separating N_2O and CO_2, and column B with 5A and 13× molecular sieve (40–60 M) for separating N_2, NO and CO.

3. Results and discussion

3.1. XRD, Raman and UV–vis

As shown in Fig. 1a, these CeO_2 powders remained in the typical cubic fluorite structure with the lattice parameters of 5.426, 5.386, 5.441, 5.415 Å, respectively. Obviously, the broad diffraction peaks for $Ce^{4+}N$ and $Ce^{4+}S$ samples indicated their small grain size (~6 nm, Table 1). CeO and $Ce^{3+}N$ samples exhibited the sharp reflections with the big grain sizes (9.5, 15.7 nm, respectively). The data in Table 1 also showed that $Ce^{4+}N$ and $Ce^{4+}S$ displayed the higher level in lattice microstrain than CeO and $Ce^{3+}N$ samples. The difference in lattice strains (caused by defects like steps, dislocations, vacancy, etc. [14]) accounted for the defect density and surface effect in $Ce^{4+}N$ and $Ce^{4+}S$ were larger than that in CeO and $Ce^{3+}N$. This effect was enhanced in ceria nanoparticles, because a larger fraction of the atoms were disordered on the surface as the particle size in reduced into nanoscale and surface atoms had reduced coordination [15].

XRD results were well complemented by Raman spectra. In Fig. 1b, these ceria materials exhibited the characteristic F_{2g} vibration band at 458 cm^{-1}. The 249 cm^{-1} band was attributed to the tetrahedral displacement of oxygen from the ideal fluorite lattice [16–18a]. Moreover, the 598 and 1174 cm^{-1} bands were linked to the oxygen vacancy or anionic defects in the imperfect fluorite structure of ceria [11,17]. According to the report [11], the band at 828 cm^{-1} was ascribed to a peroxo-like oxygen species absorbed on the oxygen vacancy. Noticeably, there was no difference in the Raman feature and position among these samples. However, the FWHM of F_{2g} line of $Ce^{4+}N$ was much bigger than that of $Ce^{3+}N$, and the value was similar between $Ce^{4+}S$ and CeO. This may be associated with either the smaller size or higher concentration of oxygen vacancy in $Ce^{4+}N$. Importantly, as shown by the I_{598}/I_{460} and $I_{(598+1174)}/I_{460}$ values in Table 1, the highest intensity ratio in $Ce^{4+}N$ (0.16) indicated that the defect concentration like oxygen vacancy reached a maximum for $Ce^{4+}N$. $Ce^{4+}S$ and CeO followed in turn, whereas $Ce^{3+}N$ showed the minimum (0.08). Therefore, a comparison of XRD and Raman results replied that the cerium precursor greatly influenced the particle size and/or surface oxygen vacancy concentration of CeO_2, whereas not on its crystalline structure.

In Fig. 2, the broad band at 352 nm ascribed to the $O^{2-} \rightarrow Ce^{4+}$ interband-transfer transition, was obviously seen in $Ce^{4+}N$, $Ce^{4+}S$ and CeO samples, whereas was not detected in $Ce^{3+}N$ sample. The 276 and 232 nm bands in the UV range appeared in all the samples, which were attributed to $O^{2-} \rightarrow Ce^{4+}$ and $O^{2-} \rightarrow Ce^{3+}$ charge-transfer transition, respectively [7]. Hence, the above observation suggested that the surface cerium species were mostly in

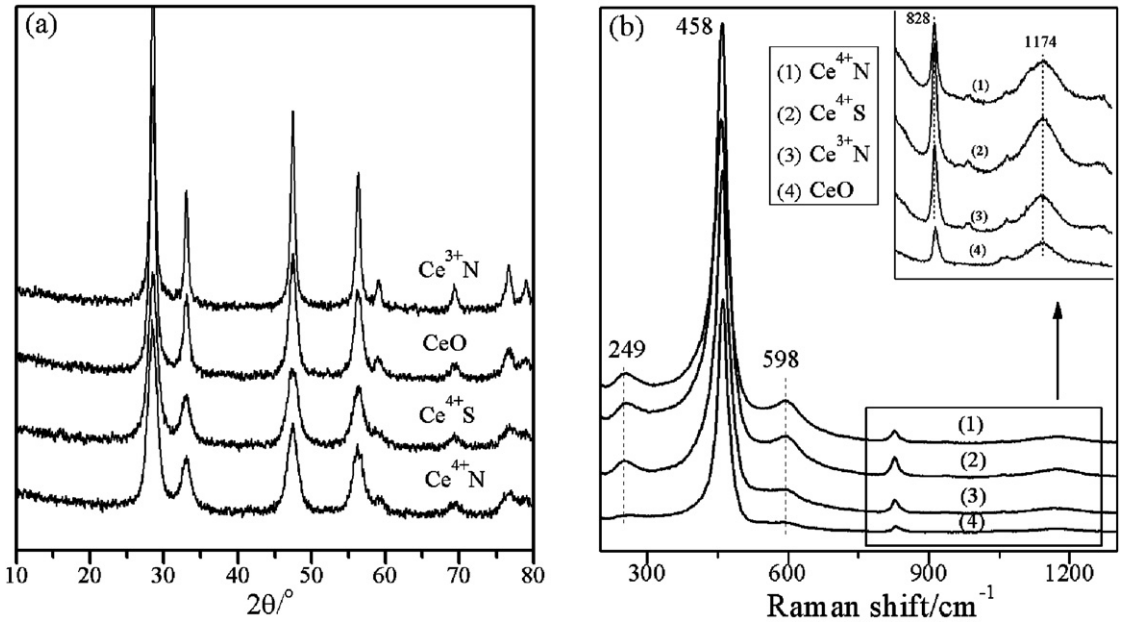

Fig. 1. XRD patterns (a) and Raman spectra (b) for CeO_2 from different precursors.

Table 1
The grain size, lattice parameter, microstain, full width at half maximum (FWHM), and the intensity ratio of Raman bands at 460, 598 and 1174 cm^{-1} for these CeO_2 from different cerium precursors.

Samples	Grain size (nm)	Lattice parameter (Å)	Microstrain (%)	I_{598}/I_{460}	$I_{(1174+598)}/I_{460}$	FWHM (cm^{-1})
$Ce^{4+}N$	5.7	5.426	1.38	0.11	0.16	37.3
$Ce^{4+}S$	5.8	5.386	1.35	0.08	0.12	32.9
CeO	9.3	5.441	0.85	0.06	0.13	32.5
$Ce^{3+}N$	15.7	5.415	0.50	0.04	0.08	28.4

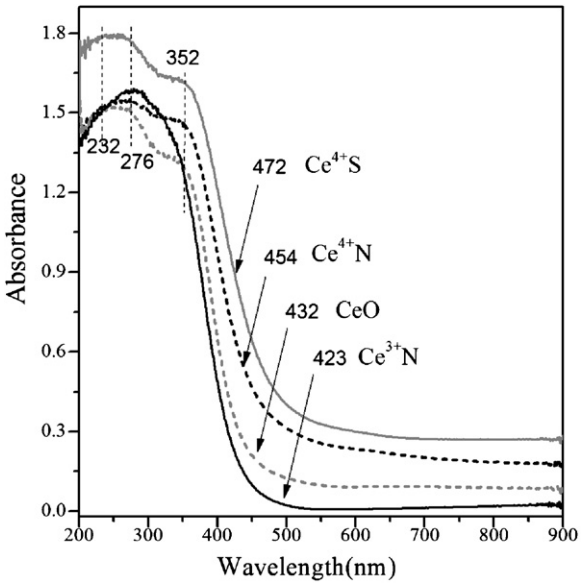

Fig. 2. UV–vis spectra for CeO_2 from different precursors.

a +4 oxidation state. This was also determined by XPS (data not shown). Moreover, the absorption edge shifted in turn from 472 to 453, 432, 423 nm with the change of $Ce^{4+}S$, $Ce^{4+}N$, CeO and $Ce^{3+}N$. The blue shifting reflected that the electronic band structures of ceria were distinguishably modified by different cerium precursors.

3.2. TEM and HRTEM

The morphology and particle size can be directly determined by TEM. As shown in Fig. 3, CeO_2 prepared from $(NH_4)_2Ce(NO_3)_6$ and $Ce(SO_4)_2$ were irregular small particles with the size of 4–6 nm (a, b), and from $Ce(NO_3)_3$ (d) showed the rod-like morphology, 100–300 nm in length and ~10 to 20 nm in diameter, whereas from CeO_2 powder (c) represented the mixed rods and particles. In fact, the aggregation of nanoparticles was due to the shrinkage of the exposed planes in order to reduce the surface energy [8b]. According to the reports [2,3,5], Ce^{3+} ions played an important role in nanorod growth. $Ce(OH)_3$ nuclei acted as the essential intermediate to self-assembly rod-like nanocrystals because of its large structural anisotropy. Whereas, tetravalent cerium ions favorably promoted the formation of spherical particles, possibly due to the reason that less-soluble and less-anisotropic CeO_2 nuclei, instead of anisotropic $Ce(OH)_3$, were formed directly when Ce^{4+} ions hydrolyzed in the basic solution [3].

The shape and orientation of ceria was further characterized by HRTEM. Take $Ce^{4+}N$ as an example (Fig. 4a), the crystallites were well aligned along [1 1 0] crystallographic direction. The predominantly exposed planes were proposed as the (1 1 1) with a small amount of (2 0 0) planes at 0.309 and 0.27 nm, respectively. $Ce^{4+}S$ (Fig. 4b) displayed the typical spherical-shape with the interplanar spacing of 0.307 nm, while CeO (Fig. 4c) was present as sheet-like enclosed by (1 1 1) planes. Concerning $Ce^{3+}N$ nanorods (Fig. 4d), its surface seemed smooth, and its growth direction was also expected along the [1 1 0] orientation. The HRTEM image displayed the dominant (1 1 1) lattice fringes with the interplanar spacing of 0.309 nm. These analyses were in agreement with the similar reports [1–8]. Accordingly, the predominantly exposed

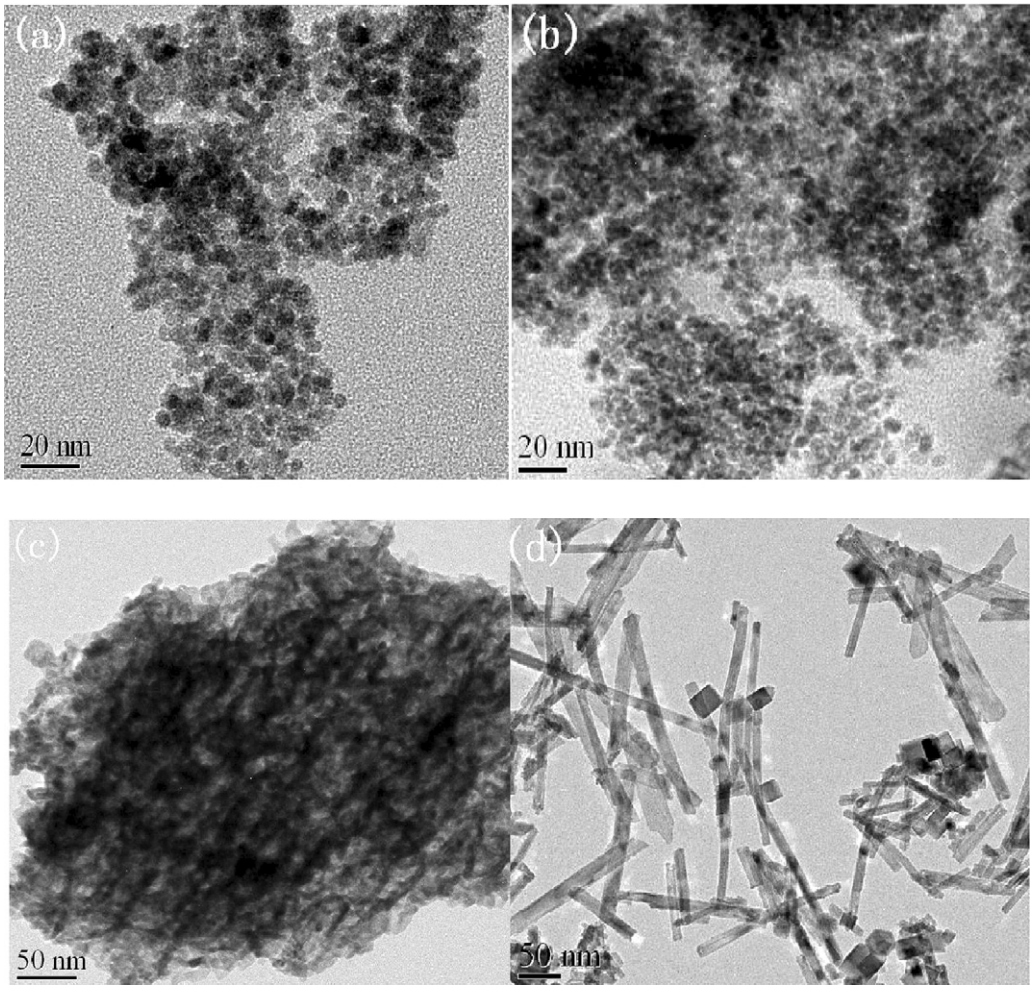

Fig. 3. TEM images for CeO_2 from different precursors (a) $(NH_4)_2Ce(NO_3)_6$, (b) $Ce(SO_4)_2$ (c) CeO_2, (d) $Ce(NO_3)_3$.

planes were reasonably indicated as the (1 1 1) in these CeO_2 nanomaterials.

3.3. H_2-TPR

Fig. 5 showed the H_2-TPR profiles of CeO_2 from different cerium precursors. For $Ce^{4+}N$ sample, the first peak started from 200 °C and exhibited the maximum intensity near 400 °C, which was attributed to the reduction of surface oxygen species at the low activation energy [4,8a,17]. Li et al. [1c] assigned the two low-temperature peaks to the reduction of surface capping oxygen in flower-like CeO_2. However, the influence of trace surface carbonate-like and other adsorbed species on the reduction property cannot be ruled out. The weak shoulder below 400 °C on CeO sample may partially originate from these impurities [17]. The second peak at high temperature centered at 750 °C was related to the reduction of bulk oxygen in ceria lattice, which likely involved slow lattice oxygen diffusion [8a]. For $Ce^{3+}N$ sample, the reduction temperature of surface oxygen layer (500 °C) was higher than that of other three ones. These results demonstrated that ceria prepared from tetravalent cerium salt were more easily to reduce than that from the tervalent nitrate. The promoting reduction behavior of $Ce^{4+}N$ and $Ce^{4+}S$ should be due to their small particle size. The surface atoms in the nanosize (4–6 nm) structure had the unsaturated coordination, which can significantly improve the intrinsic reducibility of Ce^{4+}/Ce^{3+} couple with the formation of surface oxygen vacancy. This is consistent with the reported overall trend that larger ceria particles were more difficult to reduce [1a].

3.4. Activity and selectivity

Fig. 6 compared the activity and selectivity of ceria nanocrystals toward NO reduction by CO. In the temperature range of 225–375 °C, the highest NO conversion was observed for $Ce^{4+}N$ according to the order of $Ce^{4+}N > Ce^{4+}S > CeO > Ce^{3+}N$. For example, $Ce^{4+}N$ can convert 45% and 69% NO at 275 and 350 °C, whereas only 5% and 40% conversion occurred over $Ce^{3+}N$ at the same temperature. In addition, the highest N_2 selectivity was always obtained on $Ce^{4+}N$ sample, but almost the identical was present on other three ones. Since all the preparation conditions were same (the only difference was the change of cerium precursors), the unusual results must originate from the nature of material itself. The exposed crystal planes of these samples should not be the most essential factor for determining the activity, because they almost exposed the same (1 1 1) planes. As reported elsewhere [9,10,12], oxygen vacancy in ceria played a key role in the adsorption and dissociation of NO molecules. In this way, nanosize effect should be considered primarily due to its spontaneous transformation of Ce^{4+} to Ce^{3+} upon the production of oxygen vacancy. As evidenced by above XRD, Raman and H_2-TPR results, $Ce^{4+}N$ particles associated with the smallest size and highest lattice strain had the greater ability to facilitate the formation of extrinsic oxygen vacancy, while difficult

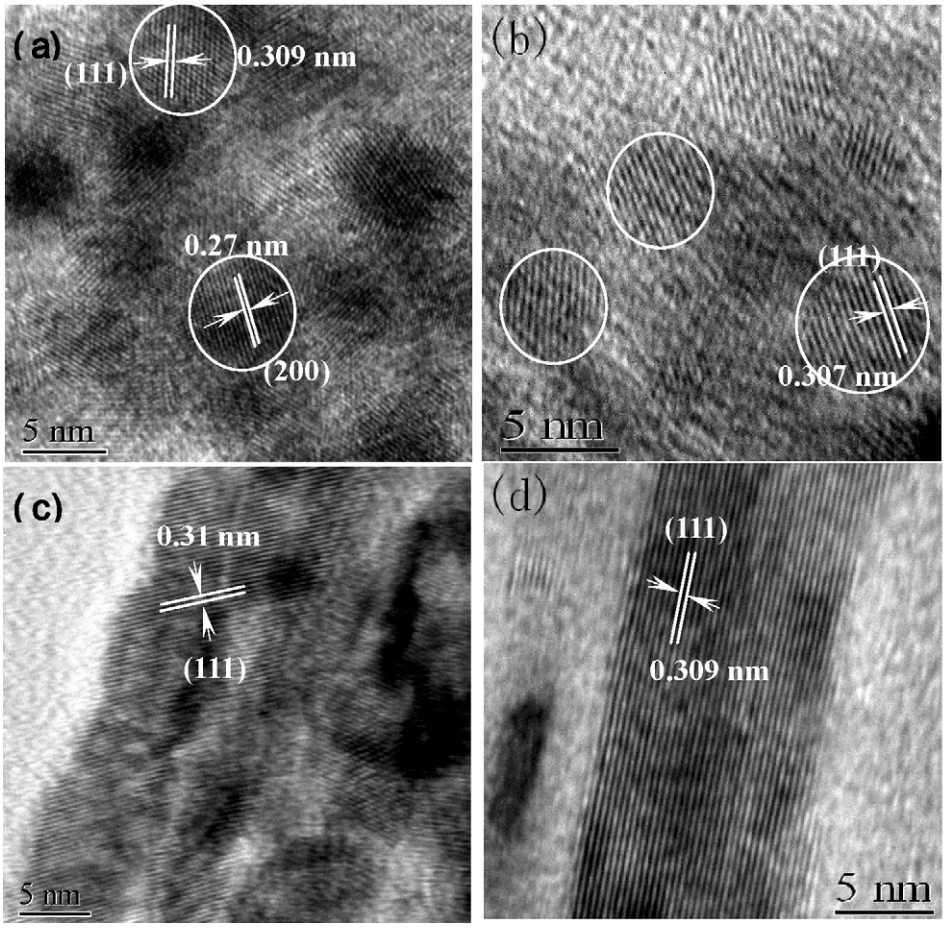

Fig. 4. HR-TEM images for CeO_2 from different precursors (a) $(NH_4)_2Ce(NO_3)_6$, (b) $Ce(SO_4)_2$, (c) CeO_2, (d) $Ce(NO_3)_3$.

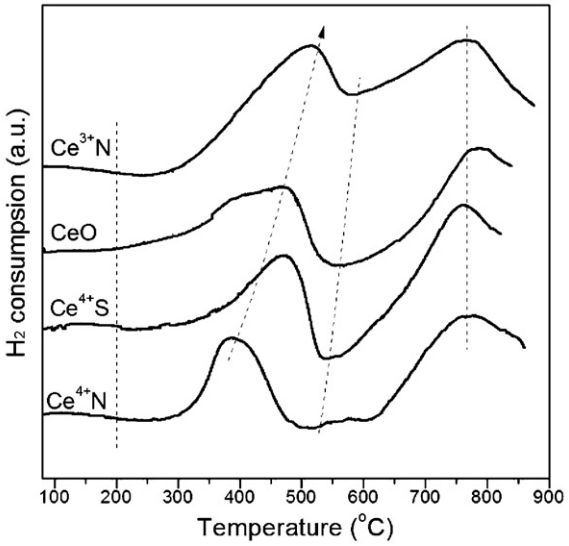

Fig. 5. H_2-TPR profiles for CeO_2 from different precursors.

for $Ce^{3+}N$ nanorods with big size and low strain. Therefore, the differences in the capacity to form this surface oxygen vacancy could result in the different activity, which depended on the shapes and particle sizes of ceria nanocrystals.

3.5. In situ FTIR of NO + CO

In situ FTIR was carried out to identify the intermediates and population of absorbed NO and CO under the simulative reaction conditions, as shown in Fig. 7a and b. Compared with CO molecule, NO preferentially interact with $Ce^{4+}N$ and $Ce^{3+}N$ samples at low temperature. As reported elsewhere [18], the main adsorption pathway involved the reaction of NO with bridged (II) OH groups to produce adsorbed H_2O–HNO_2 complexes and their decomposition products, namely NO_2^-, NO^-, and/or HNO^- species. This interaction, in principle, was described as: $2Ce^{4+}–OH^- + NO \rightarrow 2Ce^{4+}–ONO^- + H_2O$. Take $Ce^{4+}N$ as an example at room temperature, the validity of NO interaction with hydroxyl groups was proved by the disappearance of the 3662 cm^{-1} OH band and not only the appearance of nitrite at 1180–1280 cm^{-1}, but also the synchronous growth of absorptions near 3200–3600 cm^{-1} due to H-bonded water molecules (data no shown). In the region of 1000–1700 cm^{-1}, the adsorbed NO species as kinds of nitrates were formed under the oxidized formats, because NO can favorably bond to active oxygen species from ceria surface [16]. These NO species were ranging from bridge nitrate (1613–1618 cm^{-1}) to monodentate nitrate (1457–1475, 1230–1245, 1000–1020 cm^{-1}) and bidentate nitrate (1540–1555, 1280–1281, 1010–1060 cm^{-1}) [16,18,19]. In addition, NO molecule can accept an electron from the donation of reduced state cerium to form NO^- species, which easily dimerized into hyponitrites at 1360 and 1080 cm^{-1} [18a]. These species appeared on $Ce^{3+}N$. In the region of 3000–4000 cm^{-1}, for $Ce^{3+}N$ sample, the characteristic band at 3502 cm^{-1} was assigned to cerium oxyhydroxide impurities within the ceria pores [18a].

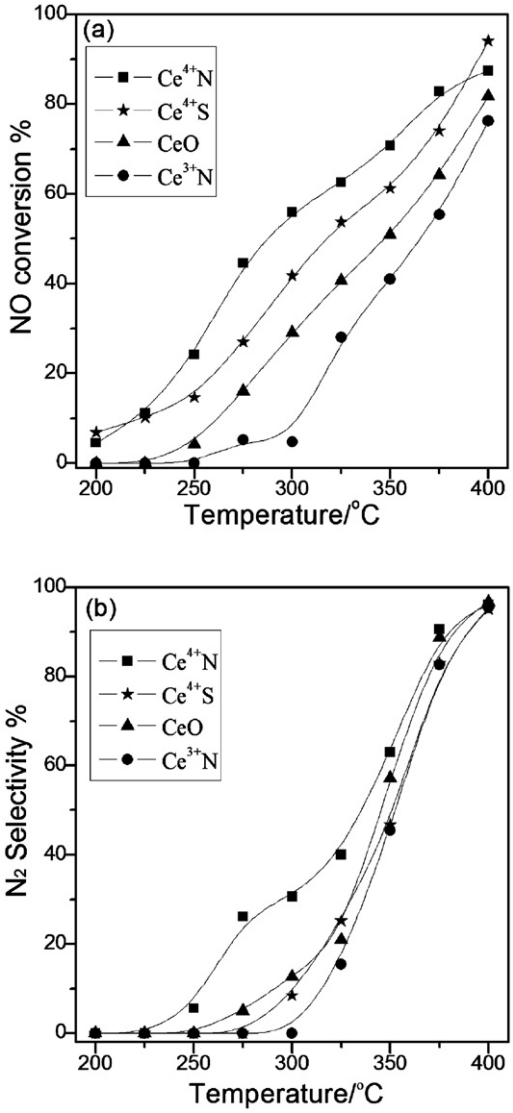

Fig. 6. (a) NO conversion (b) N_2 selectivity and N_2 yield over CeO_2 from different precursors as a function of temperature.

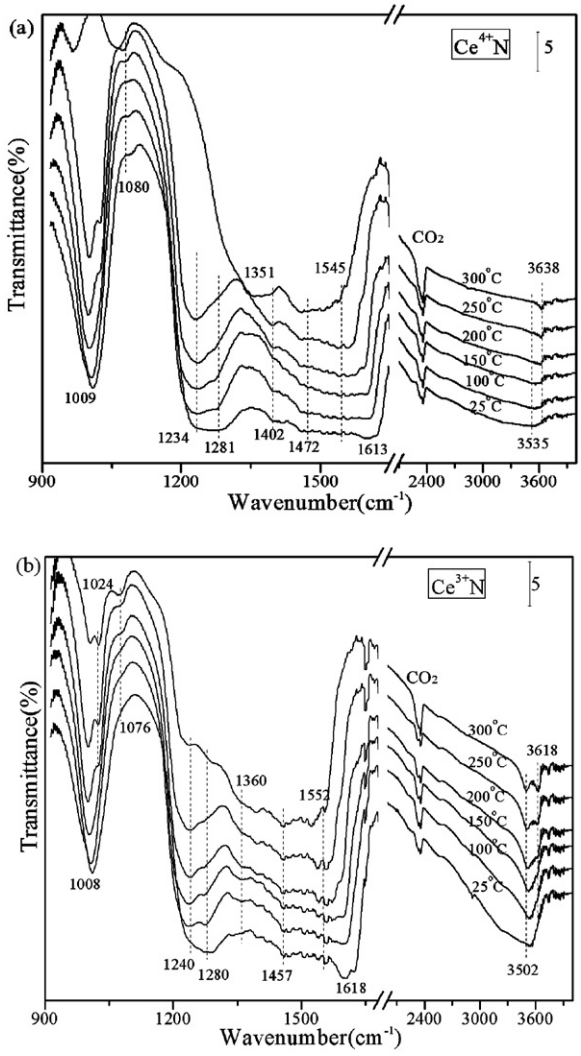

Fig. 7. In situ FTIR spectra of NO + CO interaction with $Ce^{4+}N$ (a) and $Ce^{3+}N$ (b) as a function of temperature.

Whereas, the 3535 cm^{-1} band was very weak for $Ce^{4+}N$ sample. The above findings suggested that the cerium precursors had little influence on the adsorption configuration and type of NO species.

The most important results were the evolution of the adsorbed NO species after heat treatment. For $Ce^{4+}N$ sample, bridge nitrate was not stable and disappeared at 200 °C. As the temperature was raising up to 300 °C, the initial NO_x species including monodentate, bidentate nitrate and chelating nitrite vanished completely. Subsequently, bidentate nitrates and carbonates were accumulated at 1075, 1351 and 1520 cm^{-1}. The band intensity of CO_2 also increased at 300 °C. However, regarding $Ce^{3+}N$ sample, the bands at 1008, 1240, 1280, 1457, 1552 and 3502 cm^{-1} did not completely disappear even at 300 °C, indicating these species were relatively stable on the $Ce^{3+}N$ surface. The 3300–3560 cm^{-1} hydroxyl groups gradually decreased with increasing temperature, while the 3618–3638 cm^{-1} triply bridged OH appeared above 200 °C, and its intensity increased with the increase of temperature. According to the report [18], one possibility for the lost of bridged OH groups was activation of NO by reactive oxygen at higher temperature like $NO + O^* \rightarrow NO_2$. The resulting species participated in the formation of nitrates upon interaction with basic/neutral hydroxyls, $2OH^- + 3NO_2 \rightarrow 2NO_3^- + NO + H_2O$. However, there was no enough evidence for this deduction in the present work. Therefore, the lost of 3300–3550 cm^{-1} band might be resulted from the desorption of oxy-hydroxyl or hydroxycarbonates by thermal treatment. In addition, the removal of adsorbed NO species from the surface above 200 °C may result in the re-presence of bridged OH groups. Moreover, increasing the temperature to 300 °C promoted the hyponitrite to its maximum intensity, which was considered as the candidate for the formation of N_2O at low temperature [16]. Comparatively, $Ce^{4+}N$ particles in the nanoscale (4–6 nm) showed the greater ability than $Ce^{3+}N$ rods to activate NO molecules, which was hence beneficial to its better catalytic performance. Overbury at al. [12b] also reported that interaction of NO with ceria depended upon temperature and oxidation state and to lesser extent upon the crystallographic orientation of ceria.

A possible reaction mechanism was proposed, as shown in Fig. 8. When both NO and CO molecules were introduced into the reactor, NO was adsorbed in combination with surface oxygen to form nitrate or nitrite. CO took away the active oxygen, resulting in the formation of CO_2 and surface oxygen vacancy (SOV). CO reduction of surface oxygen was proposed to be the first and crucial step on NiO/CeO_2 catalyst [19]. The adsorbed NO species will be dissociated by the adjacent SOV to form N* and O*. The SOV would be filled by O* to regenerate the surface oxygen atoms. N* can react with N* or NO to produce N_2 or N_2O. Actually, we did such an experiment

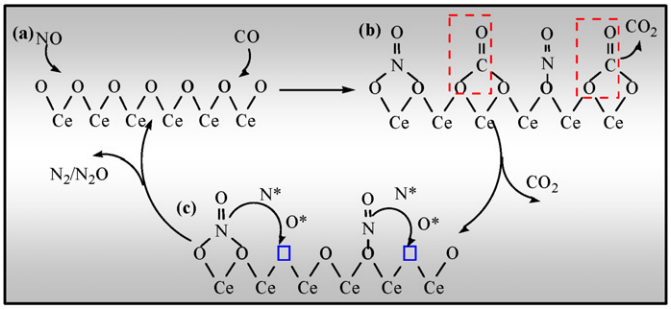

Fig. 8. The possible reaction mechanism of NO + CO over nanoscale ceria.

to support this deduction. CeO_2 sample was firstly pretreated by CO at 300 °C for 15 min. As a result, CO_2 was detected by GC, and the yellow CeO_2 was turned to gray. Subsequently, the sample was purified by flowing He, and then NO was introduced. It was found that the color of CeO_2 was recovered from gray to yellow, and N_2O was detected. Therefore, it was believed that NO dissociation was promoted by SOV. The formation capacity of oxygen vacancy should play a central role in determining the NO reduction activity.

4. Conclusion

The present work demonstrated that the cerium precursors greatly influenced the morphology and size of ceria. However, the predominantly exposed plane of them was mainly indicated as the (1 1 1). As compared with nanorods prepared from $Ce(NO_3)_3$, CeO_2 nanoparticles from $(NH_4)_2Ce(NO_3)_6$ with an average size of 4–6 nm and larger lattice strain, showed the higher activity for NO reduction. This was primarily due to the nanosize effects that improved its intrinsic reducibility of surface oxygen and facilitated the formation of oxygen vacancies significantly. In addition, the adsorption type of NO was similar over the different shaped ceria. However, CeO_2 nanoparticles from tetravalent cerium showed the greater capacity to activate the adsorbed NO species than nanorods from the tervalent nitrates.

Acknowledgements

The financial supports of the National Natural Science Foundation of China (Nos. 20873060, 20973091) and the National Basic Research Program of China (No. 2010CB732300) are gratefully acknowledged.

References

[1] (a) K.B. Zhou, X. Wang, X.M. Sun, Q. Peng, Y.D. Li, J. Catal. 229 (2005) 206;
(b) X.W. Liu, K.B. Zhou, L. Wang, B.Y. Wang, Y.D. Li, J. Am. Chem. Soc. 231 (2009) 3140;
(c) H.F. Li, G.Z. Lu, Q.G. Dai, Y.Q. Wang, Y. Guo, Y.L. Guo, Appl. Mater. Interface 2 (2010) 838;
(d) C.J. Mao, Y.X. Zhao, X.F. Qiu, J.J. Zhu, C. Burda, Phys. Chem. Phys. Chem. 10 (2008) 5633;
(e) G.A. Deluga, J.R. Salge, D.L. Schmidt, X.E. Verykios, Science 303 (2004) 993.
[2] C.S. Pan, D.S. Zhang, L.Y. Shi, J.H. Fang, Eur. J. Inorg. Chem (2008) 2429.
[3] H.X. Mai, L.D. Sun, Y.W. Zhang, R. Si, W. Feng, H.P. Zhang, H.C. Liu, C.H. Yan, J. Phys. Chem. B 109 (2005) 24380.
[4] M.L. Tana, J. Zhang, H.J. Li, Y. Li, W.J. Li, Shen, Catal. Today 148 (2009) 179.
[5] C.C. Tang, Y. Bando, B.D. Liu, D. Golgerg, Adv. Mater. 17 (2005) 3005.
[6] W.Q. Han, L.J. Wu, W.M. Zhu, J. Am. Chem. Soc. 127 (2005) 12814.
[7] C.M. Ho, J.C. Yu, T. Kwong, A.C. Mak, S. Lai, Chem. Mater. 17 (2005) 4514.
[8] (a) J.H. Xu, J. harmer, G.Q. Li, T. Chapman, P. Collier, S. Longworth, S.C. Tsang, Chem. Comm. 46 (2010) 1887;
(b) Z.L. Wang, X.D. Feng, J. Phys. Chem. B 107 (2003) 13563.
[9] S. Roy, M.S. Hegde, G. Madras, Appl. Energy 86 (2009) 2283.
[10] M. Nolan, S.C. Parker, G.W. Watson, Surf. Sci. 595 (2005) 223.
[11] Y.M. Choi, H. Abernathy, H.T. Chen, M.C. Lin, M.L. Liu, ChemPhysChem 7 (2006) 1957.
[12] (a) M. Nolan, S.C. Parker, G.W. Watson, J. Phys. Chem. B 110 (2006) 2256;
(b) S.H. Overbury, D.R. Mullins, D.R. Huntley, L.J. Kundakovic, J. Catal. 186 (1999) 296.
[13] A. Gayen, T. Baidya, G.S. Ramesh, R. Srihari, M.S. Hegde, J. Chem. Sci. 118 (2006) 47.
[14] R. Si, M. Flytzani-Stephanopoulos, Angew. Chem. 120 (2008) 2926.
[15] P. Dutta, S. Pal, M.S. Seehra, Chem. Mater. 18 (2006) 5144.
[16] B. Azambre, L. Zenboury, F. Delacroix, J.V. Weber, Catal. Today 137 (2008) 278.
[17] N. Guillén-Hurtado, I. Atribak, A. Bueno-Lopez, A. García-García, J. Mol. Catal. A: Chem. 323 (2010) 52.
[18] (a) B. Azambre, L. Zenboury, A. Koch, J.V. Weber, J. Phys. Chem. C 113 (2009) 13287;
(b) B. Azambre, I. Atribak, A. Bueno-Lopez, A. Garacía-García, J. Phys. Chem. C 114 (2010) 13300.
[19] X.Q. Cheng, A.M. Zhu, Y.Z. Zhang, Y. Wang, C.T. Au, C. Shi, Appl. Catal. B: Environ. 90 (2009) 395.